Journal of Photochemistry and Photobiology 12 (2022) 100154

Contents lists available at ScienceDirect

Journal of Photochemistry and Photobiology

journal homepage: www.sciencedirect.com/journal/journal-of-photochemistry-and-photobiology

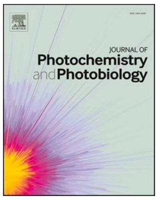

Energy transfer in supramolecular calix[4]arene—Perylene bisimide dye light harvesting building blocks: Resolving loss processes with simultaneous target analysis

Ivo H.M. van Stokkum [a,*], Catharina Wohlmuth [b], Frank Würthner [b], René M. Williams [c,*]

[a] *Department of Physics and Astronomy and LaserLaB, Faculty of Science, Vrije Universiteit, de Boelelaan 1081, 1081 HV Amsterdam, the Netherlands*
[b] *Institut für Organische Chemie, Universität Würzburg, Am Hubland, D-97074 Würzburg, Germany*
[c] *Molecular Photonics Group, van't Hoff Institute for Molecular Sciences (HIMS), Universiteit van Amsterdam, Science Park 904, 1098 XH Amsterdam, the Netherlands*

ARTICLE INFO

Keywords:
Transient absorption spectroscopy
Fluorescence resonance energy transfer
Photoinduced electron transfer
Species associated difference spectrum
Excitonic interaction

ABSTRACT

By the application of simultaneous target analysis of multiple femtosecond transient absorption data sets we have identified two loss channels within multi-chromophoric light harvesting arrays. Perylene bisimide-calix[4]arene arrays composed of up to three different types of perylene bisimide (PBI) chromophores, orange (**o**), red (**r**), and green (**g**) PBIs (named after their colors as solids), have previously been studied by transient absorption spectroscopy (Hippius et al., J. Phys. Chem C 112:2476, 2008) and here we present a simultaneous target analysis of those data matrices. A covalent system containing the red chromophore (**r**) and calix[4]arene (**c**), the **rc** system, shows extensive spectral evolution that can be described with four excited states ($\mathbf{r_1}^*\rightarrow\mathbf{r_2}^*\rightarrow\mathbf{r_3}^*\rightarrow\mathbf{r_4}^*\rightarrow$ground state). In the Perylene Orange calix[4]arene system (**oc**), a radical pair (**oc**RP) can be formed by photoinduced electron transfer (Hippius et al., J. Phys. Chem C 111:13988, 2007). In a simultaneous target analysis of the multichromophoric systems **ocr, rcocr** and **ocrco** the properties of **rc** and **oc** are integrated, and excitation energy transfer (EET) from **o*** to **r*** occurs. In addition, we demonstrate that the final Species Associated Difference Spectrum (SADS) also contains **o** bleach features that indicate an excitonic interaction, for **ocr, rcocr** and **ocrco**. In a simultaneous target analysis of **rcg** and **gcrcg** the properties of **rc** are integrated, and next to EET to **g*** we can resolve the formation of a new **rcgRP** that is formed from $\mathbf{r_1}^*$ or $\mathbf{r_2}^*$, and represents a loss of 7 and 12%, respectively. In a simultaneous target analysis of **ocrcg** the properties of **ocr** and **rcg** are integrated, arriving at a consistent picture with an energy transfer quantum yield of formation of the excited state of the green PBI (**g***) of 80%.

Introduction

The sun is a huge source of energy [1] and there is a tremendous range of options to exploit this [2–4]. Next to using the sun to create heat with a solar furnace [5] that drives energy storing reactions, also photovoltaic technologies based on for instance organic [6–10], dye sensitized [11–13], perovskite [14–19], gallium arsenide [20–22] semi-conductors or on the more widespread black silicon [23, 24] are ubiquitous. Electrical power thus generated in a sustainable way can be coupled to efficient electrolysers [25, 26] to create hydrogen-gas [17] as a chemical energy storage medium. By focussing on the molecular approach [27–30], we can apply tuneable molecular properties [31] combined with molecule based [32] catalytic systems [33] to split water and reduce carbon dioxide in one organized assembly, similar to natural photosynthesis. The primary event in these molecule-based energy conversion systems is light harvesting. Molecular components that can interact and funnel the exciton energy to a catalytic location thus are essential units. The efficient transfer of excited state energy thereby contributes to the overall output of the system and therefore loss channels should be identified. Time-resolved laser spectroscopy in combination with global and target analysis has been used to study energy transfer in calix[4]arene – perylene bisimide (PBI) dye building blocks [34–36]. Although these chromophores are excellent light harvesters (Fig. 1A), competing charge transfer processes [34] reduce the efficiency, which has been demonstrated in **oc** containing compounds [34, 35]. Thus, in 2008 we arrived at the kinetic scheme of Fig. 1B for

---

* Corresponding authors.
E-mail addresses: i.h.m.van.stokkum@vu.nl (I.H.M. van Stokkum), r.m.williams@uva.nl (R.M. Williams).

https://doi.org/10.1016/j.jpap.2022.100154

the tri-chromophoric supramolecular system **ocrcg**.

The parent core-unsubstituted **o** PBI chromophore absorbs well around ≈500 nm, and transfers its energy to the tetraphenoxy-substituted **r** PBI chromophore in ≈1.4 ps ($k_{\mathrm{EET}} \approx 7.1 \times 10^{11}\mathrm{s}^{-1}$). In turn, the **r** chromophore transfers its energy to the dipyrrolidino-substituted **g** PBI chromophore in ≈1.8 ps ($k_{\mathrm{EET}} \approx 5.5 \times 10^{11}\mathrm{s}^{-1}$). In the **ocg** system the **o** PBI chromophore can also transfer its energy to the dipyrrolidino-substituted **g** PBI chromophore with $k_{\mathrm{EET}} \approx 1.5 \times 10^{11}\mathrm{s}^{-1}$, slightly slower due to a reduced spectral overlap. Due to the large energy gaps between **o** and **r**, and between **r** and **g**, all three downhill energy transfers are virtually unidirectional, and the uphill energy transfers can safely be ignored. These rate constants for the downhill energy transfers are in very good agreement with those calculated according to the Förster theory [35]. As a competitive process we reported in our previous study [34] that the excited **o** chromophore can accept an electron from the calix (rate constant (12 ps)$^{-1}$, $k_{\mathrm{PET}} \approx 8.3 \times 10^{10}\mathrm{s}^{-1}$), resulting in a $\mathbf{c}^{+\cdot}\mathbf{o}^{-\cdot}$ radical ion pair (RP), that in turn decays by charge recombination to the triplet and to the ground state. However, according to our recent re-investigation, this picture is incomplete. Here, with the help of simultaneous target analysis of supramolecular systems we demonstrate that the **r** and **g** chromophores interact resulting in a $\mathbf{r}^{-\cdot}\mathbf{c}^{+\cdot}\mathbf{g}$ radical ion pair (**rcgRP**), thus representing an additional loss process that limits the light harvesting efficiency of calix[4]arene – perylene bisimide dye building blocks.

Materials and methods

The chemical structures of the PBI–calix[4]arene conjugates and the reference compounds studied are collated in Figure S 1. The chemical structures of the di- and tri-chromophoric supramolecular systems **ocr, rcocr, ocrco, rcg, rcgcr, gcrcg, ocg, ocrcg** and of **gcrcocrcg** (five chromophores) studied here are collated in Fig. 2. The dichromophoric supramolecular systems **oco, rcr** and **gcg** are depicted in Figure S 2. For all details on the synthesis and the characterization of the compounds and for the transient absorption spectroscopy methods we refer to [34–37].

Briefly, transient absorption spectra were measured at magic angle from 380 to 852 nm at 335 time delays between −1 and 910 ps. The excitation pulse was centered at 530 nm, and the full width at half maximum (FWHM) of the instrument response function (IRF) was ≈120 fs. The laser output was typically 5 mJ per pulse, and the maximum amplitude of the difference absorption signals was ≈100 mOD. Samples were prepared to have an optical density of *ca.* 0.3–0.6 at the excitation wavelength and were degassed for 15 min with argon gas prior to the measurements. The UV/vis absorption spectra of the samples were measured before and after the laser experiments, and the spectra were virtually identical, thus possible degradation or chemical change of the samples could be ruled out. Here we briefly summarize the simultaneous target analysis method that is key to this paper.

In target analysis [38, 39] of transient absorption data, the inverse problem is to determine the number of electronically excited states (N_{states}) present in the system, to estimate their populations $c_l^S(t)$(superscript S stands for species), and the species' spectral properties, the Species Associated Difference Spectra ($SADS_l(\lambda)$), where λ is the wavelength. The Time Resolved Spectra (TRS) are described by:

$$TRS(t,\lambda) = \sum_{l=1}^{N_{states}} c_l^S(t',\theta) SADS_l(\lambda)$$

where the populations are determined by an unknown compartmental model, which depends upon the unknown kinetic parameters θ. In the target analysis, constraints on the *SADS* are needed to estimate all parameters θ and $SADS_l(\lambda)$. t' indicates that the actual model function still has to take into account the IRF. For every wavelength, the matrix formula for this superposition model is given by [40]:

$$TRS = C^S(\theta,\mu,\Delta)\cdot SADS + IRF(\mu,\Delta)\cdot IRFAS$$

A Gaussian shaped IRF is used, with parameters μ for the time of the IRF maximum and Δ for the FWHM of the IRF. The wavelength dependence of the parameter μ is described by a second order polynomial in the wavenumber domain. The term $IRF(\mu,\Delta')\cdot IRFAS$ describes the "coherent artefact" (CA). It contains a matrix $IRF(\mu,\Delta)$ with the zeroth, first and second derivative of the IRF [40, 41]. The IRFAS amplitudes associated with each IRF derivative are wavelength dependent. The residual matrix is analysed with the help of the singular value decomposition (SVD) [38, 39]. The estimated relative precision of the estimated parameters is 10%. The parameter estimation methods are detailed in [40].

In a simultaneous target analysis of multiple experiments information can be integrated. SADS estimated from an earlier target analysis of a relatively simple system can be added as guidance spectra (GS) in a subsequent analysis of a more complicated system. We illustrate this with an example: the **rc** system shows extensive spectral evolution that can be described with four excited states $\mathbf{r_1}^*\rightarrow\mathbf{r_2}^*\rightarrow\mathbf{r_3}^*\rightarrow\mathbf{r_4}^*\rightarrow$ ground state, resulting in four rate constants $k_{r2,r1}, k_{r3,r2}, k_{r4,r3}, k_{r4}$ (where we use the $k_{to,from}$ convention, and k_{r4} denotes the decay rate to the ground state) and four **rc**-SADS. In a simultaneous target analysis of **rcg** the properties of **rc** are integrated, by adding to the **rc**-kinetic scheme the four EET to **g*** rate constants $k_{g,r_1}, k_{g,r_2}, k_{g,r_3}, k_{g,r_4}$. However, the fit using

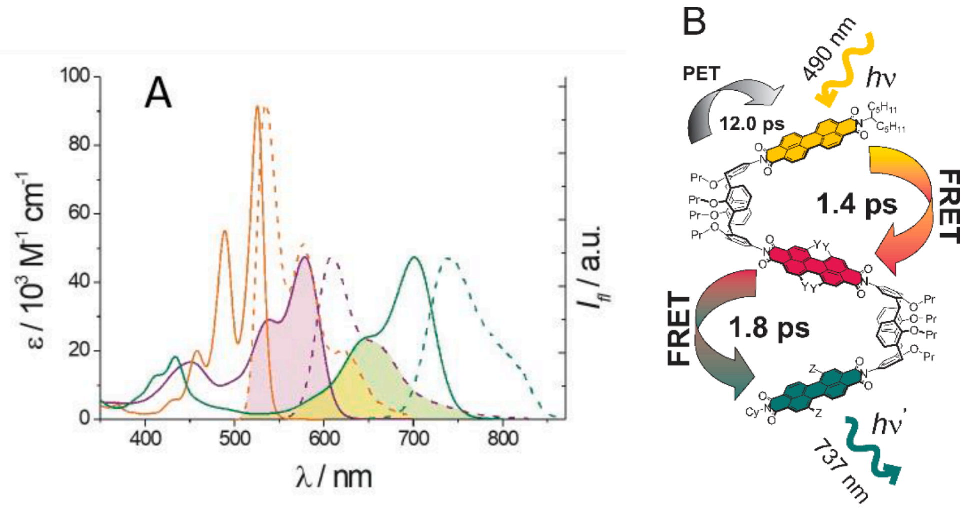

Fig. 1. (A) UV/vis absorption (orange, solid) and fluorescence emission spectra (orange, dashed) of core-unsubstituted (orange) PBI compound **oc**; UV/vis absorption (red, solid) and fluorescence emission spectra (red, dashed) of tetraphenoxy-substituted (red) PBI compound **rc**; UV/vis absorption (green, solid) and fluorescence emission spectra (green, dashed) of dipyrrolidino-substituted (green) PBI compound **gc**. For comparison, the spectral overlap for the respective dye units is highlighted by shading for the donor-acceptor pairs **o** to **r** (violet area), **r** to **g** (yellow green area), and **o** to **g** (yellow area). All spectra are taken in CH_2Cl_2. (B) Schematic representation for the processes occurring in **ocrcg** upon photoexcitation according to [35]. FRET Förster resonance energy transfer, PET photoinduced electron transfer. Figure adopted from [37].(For interpretation of the references to color in this figure legend, the reader is referred to the web version of this article.)

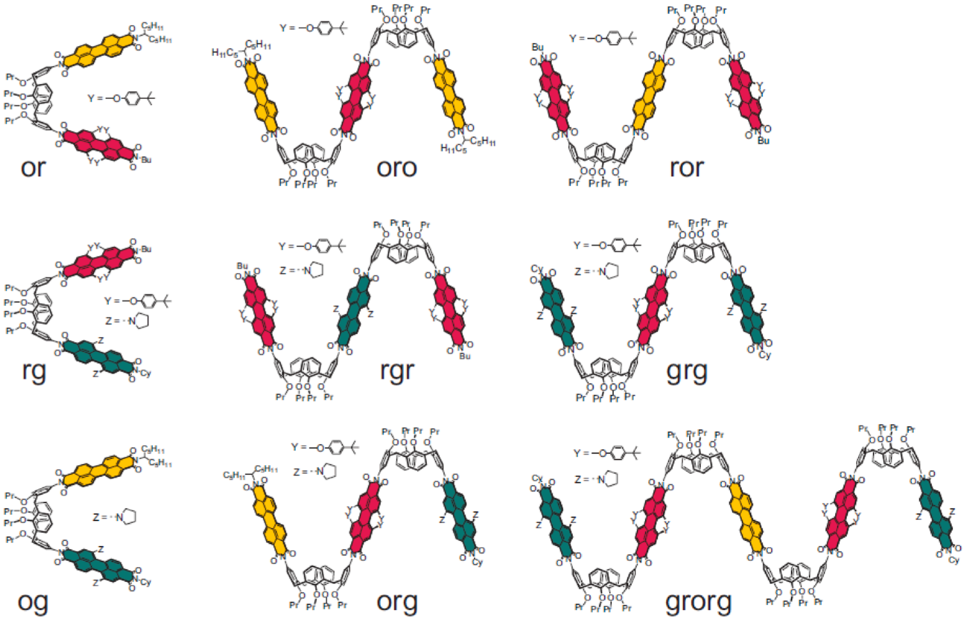

Fig. 2. Chemical structures of the supramolecular systems **ocr, ocrco, rcocr, rcg, rcgcr, gcrcg, ocg, ocrcg** and **gcrcocrcg** studied here. Figure taken from [37]. Note that the **c** is omitted from the labels in the figure.

this model is unsatisfactory (vide infra), which necessitates the introduction of a loss process: the formation of a new **rcgRP** from **r$_1$*** or **r$_2$***, which requires two new rate constants $k_{rcgRP,r1}, k_{rcgRP,r2}$. Thus the **rcg** system can be described by the four **rc**-SADS, the **g***-SADS and the **rcgRP**-SADS, and the twelve rate constants: $k_{r2,r1}, k_{r3,r2}, k_{r4,r3}, k_{r4}$; k_{g,r_1}, $k_{g,r_2}, k_{g,r_3}, k_{g,r_4}$; $k_{rcgRP,r1}, k_{rcgRP,r2}$ and the decay rates to the ground state k_g, $k_{\mathbf{rcgRP}}$. This kinetic scheme is depicted in Fig. 9. The matrix-vector notation of this simultaneous target analysis is: concentration vector $c^T(t) = [\, r_1(t) \quad r_2(t) \quad r_3(t) \quad r_4(t) \quad g(t) \quad \mathbf{rcgRP}(t) \,]$, differential equation $\frac{dc(t)}{dt} = K \cdot c(t)$ with initial concentration vector $c^T(0) = [\, 1 \quad 0 \quad 0 \quad 0 \quad 0 \quad 0 \,]$ and

$$K = \begin{bmatrix} 0 & 0 & 0 & 0 & 0 & 0 \\ k_{r2,r1} & 0 & 0 & 0 & 0 & 0 \\ 0 & k_{r3,r2} & 0 & 0 & 0 & 0 \\ 0 & 0 & k_{r4,r3} & -k_{r4} & 0 & 0 \\ k_{g,r_1} & k_{g,r_2} & k_{g,r_3} & k_{g,r_4} & -k_g & 0 \\ k_{rcgRP,r1} & k_{rcgRP,r2} & 0 & 0 & 0 & -k_{rcgRP} \end{bmatrix}$$

From the differential equation the concentration vector for each compartment is computed (taking into account the IRF) and the concentration matrix for **rcg** is given by $C^S = [\, r_1 \quad r_2 \quad r_3 \quad r_4 \quad g \quad \mathbf{rcgRP} \,]$. The **rc**-SADS (estimated from the target analysis of **rc**) are now used as guidance spectra $GS_{r1}, GS_{r2}, GS_{r3}, GS_{r4}$ and, for every wavelength, the matrix formula (omitting the IRFAS term for clarity) for the simultaneous target analysis is

$$\begin{bmatrix} TRS_{rcg} \\ GS_{r1} \\ GS_{r2} \\ GS_{r3} \\ GS_{r4} \end{bmatrix} = \begin{bmatrix} r_1 & r_2 & r_3 & r_4 & g & rcgRP \\ \alpha & 0 & 0 & 0 & 0 & 0 \\ 0 & \alpha & 0 & 0 & 0 & 0 \\ 0 & 0 & \alpha & 0 & 0 & 0 \\ 0 & 0 & 0 & \alpha & 0 & 0 \end{bmatrix} \cdot \begin{bmatrix} SADS_{r1} \\ SADS_{r2} \\ SADS_{r3} \\ SADS_{r4} \\ SADS_g \\ SADS_{rcgRP} \end{bmatrix}$$

Where α is a global scaling parameter. Thus, the results from the target analysis of the **rc** system are integrated into the target analysis of the **rcg** system. The usage of guidance spectra allows for some flexibility, to accommodate small differences in the experimental conditions or the wavelength calibration or the white light of the probe, when the experiments have been performed on different days.

Results and discussion

Spectral evolution in oref, rref, gref, rc, crc, gc and cgc

The reference chromophores **oref, rref** and **gref** (see Figure S 1 for the molecular structures) show an extensive spectral evolution, that can be described with four sequential compartments(Figure S 4, Figure S 5, Figure S 7, Table S 1), except for **oref** in CCl_4 which requires three sequential compartments. The **rc, crc, gc** and **cgc** complexes (see Figure S 1 for the molecular structures) behave similarly (Figure S 8, Figure S 9). Here we discuss in detail **rref** and **rc** in CH_2Cl_2 (Fig. 3). In the **rc** chromophore, a striking feature of these four SADS is the significant red shift of the maximum of the bleach (BL) plus stimulated emission (SE) signal from 585 nm to 615 nm. The first SADS (grey) can be assigned to the excited **rc** chromophore in the Franck-Condon state. The fastest solvation that can be resolved is in 0.13 ps (which is comparable to the FWHM of the IRF, 0.12 ps). The 2nd SADS (green) rises with 0.13 ps and evolves in 0.63 ps to the broader 3rd SADS (red). The redshift of the SE causes a broadening of the BL+SE band, and a somewhat smaller amplitude. The 3rd SADS decays in 6.6 ps to the final SADS (purple). Concomitantly, the excited state absorption (ESA) around 720 nm shifts to the red, visible as a shift of the iso-absorptive points from 665 to 690 nm (the crossing points with the zero-line). The lifetime of the fully relaxed and solvated **rc** chromophore is ≈2-3 ns. The estimation of this longest lifetime is hampered by the longest delay time of 910 ps, in combination with experimental limitations of the pump probe overlap. Slight changes of the alignment of the pump and the probe as a function of the delay time in the different experiments are responsible for the apparent differences in the final **r*** decay rate.

The spectral evolution is found not only in the calix[4]arene substituted compound **rc** and **crc**, but also for the pristine red reference compound **rref** (Fig. 3C,D, Figure S 5). Thus, these spectral shifts are assumed to be inherent to the chromophore itself. They might be attributed to conformational changes of the red perylene bisimide dye, a behavior which is also known from single molecule spectroscopy for the red perylene bisimides bearing phenoxy substituents at the bay positions that were immobilized in a polymer matrix. It is known that local reorganizations in the vicinity of the molecule have an impact on the orientation of the phenoxy substituents of these red PBIs. We attribute these spectral shifts to conformational changes of the phenoxy

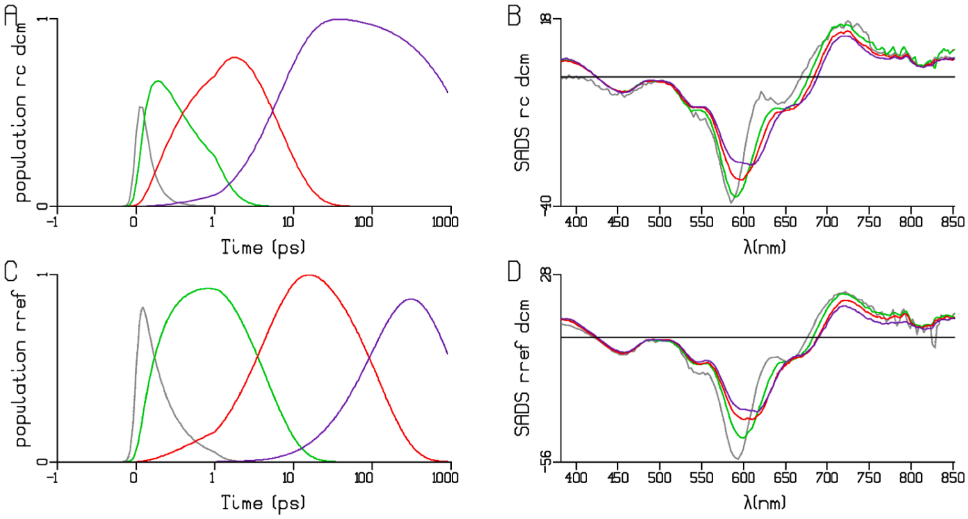

Fig. 3. Populations (A,C) and SADS (B,D, in mOD) of the four sequential compartments of **rc** and **rref** in CH_2Cl_2. Key: grey, **r*FC**: excited **r** chromophore in the Franck-Condon state; green, red, purple: successively relaxed **r*** states. Note the strong similarity of the spectra in B and D, showing the spectral evolution in time, especially from 550 to 750 nm, of the perylene red chromophore.(For interpretation of the references to color in this figure legend, the reader is referred to the web version of this article.)

substituents in the bay positions of the chromophore [42–44]. Thus, the intrinsic intricate solvation dynamics on time scales of 0.13, 0.63, and 6.6 ps will in turn complicate the analysis of experiments of systems that contain the **rc** chromophore.

The “coherent artefact” (CA) could be well described with the help of the zeroth, first and second derivative of the IRF (Figure S 6A) multiplied with the IRF Associated Spectra (Figure S 6B).

Spectral evolution in oc, coc and ocg

Traces of data and fits at selected wavelengths of **oc** and **coc** in CH_2Cl_2 after excitation at 530 nm are depicted in Fig. 4. Straddling time zero is the coherent artefact, which is described with a Gaussian shape (plus the 1st and 2nd derivative) [40, 41]. Obviously, the **o*** emission (at 571 nm) is quenched in less than 100 ps. This first loss process, which

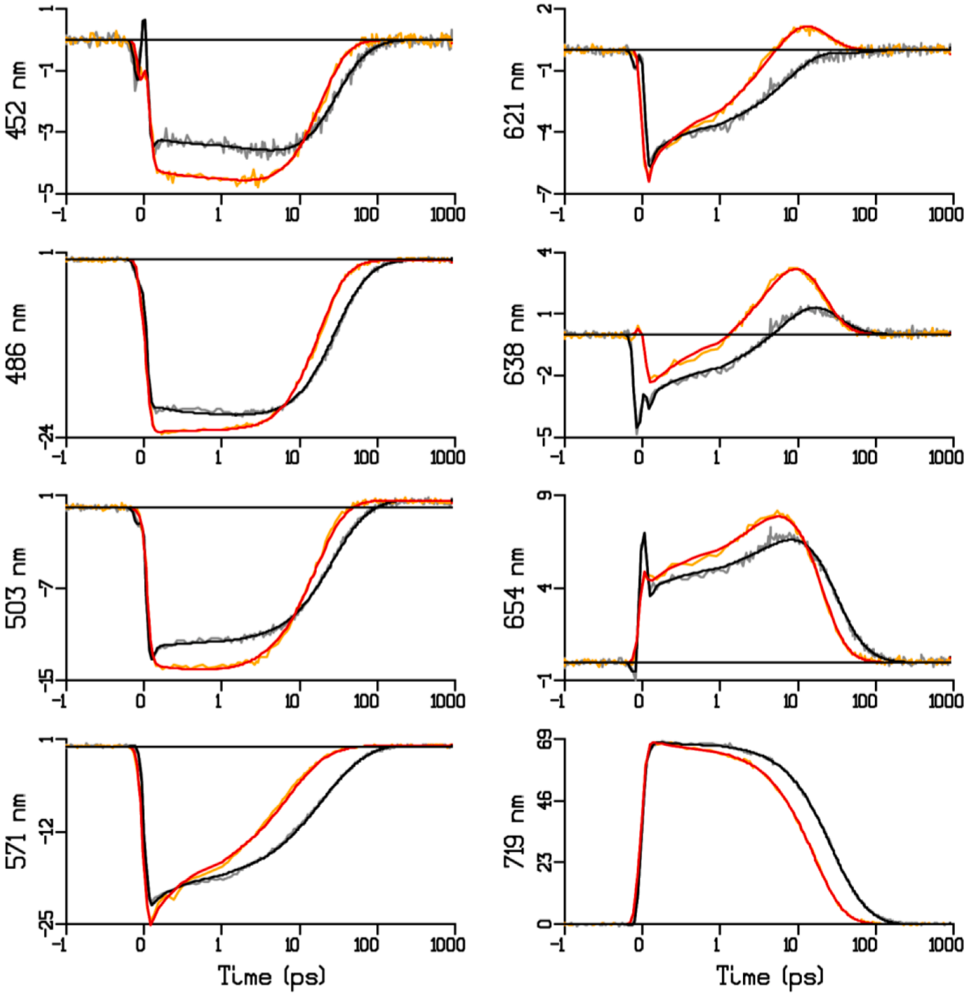

Fig. 4. Selected time traces of **oc** and **coc** in CH_2Cl_2 after excitation at 530 nm data (in mOD, grey, orange for **oc** and **coc**, respectively) and fit (black, red). Wavelength is indicated in the ordinate label. Note that the time axis is linear until 1 ps (after the maximum of the IRF), and logarithmic thereafter. The presence of two donors in coc (orange/red lines) speeds up the photoinduced electron transfer.(For interpretation of the references to color in this figure legend, the reader is referred to the web version of this article.)

has been described before [34], is the formation of an $\mathbf{c}^{+\cdot}\mathbf{o}^{-\cdot}$ radical ion pair (RP). A further complication with the **oc** complex is its heterogeneous dynamics. In CH_2Cl_2 the solvated **o*** (orange in Fig. 5A) decays with rates of 79 and 26 ns^{-1}. These two populations are almost equal, Fig. 5A. The estimated SADS of **oc** in CH_2Cl_2 (Fig. 6B) show the expected spectral evolution from the excited **o** chromophore in the Franck-Condon state (magenta, **o*FC**) to relaxed **o*** (orange). The two different conformations of **o*** have identical SADS. The $\mathbf{c}^{+\cdot}\mathbf{o}^{-\cdot}$ radical ion pair (blue, **ocRP**) consists of the bleach of **o** at 490 and 530 nm and a broad RP absorption from 600 to 850 nm. The **ocRP** partly decays via a triplet state (black SADS in Fig. 6B, cf. the 503 nm trace in Fig. 4). To resolve the SADS of **ocRP** two spectral constraints have been used, equality with the **o*** SADS from 470 to 500 nm, and the **ocRP** SADS is equated to zero from 570 to 600 nm.

In a simultaneous target analysis with **ocg** the rates of excitation energy transfer from the different **o*** compartments to **g** can be estimated. The **o*** with the fastest rate of RP formation shows a slower EET rate to the **g** chromophore (129 vs. 186 ns^{-1}. Note that a rate of 100 ns^{-1} corresponds to an energy transfer rate of $k_{EET} = 1 \times 10^{11}\ s^{-1}$). This could be due to different steric factors in the Förster equation for EET. From the kinetic schemes of **oc** and **ocg** in the three solvents (Figure S 10) several trends can be discerned. In **coc**, where two calix[4]arenes are connected to **o**, the rates of **ocRP** formation are assumed to be twice as large. This describes the data well (Fig. 4), however, the fractions are different in CH_2Cl_2. In toluene and benzonitrile the **o*** fraction with a large rate of **ocRP** formation is ≈20%, and the rate of EET to **g*** is only ≈50 ns^{-1}. In contrast, the **o*** fraction with a smaller rate of **ocRP** formation shows a rate of EET to **g*** of ≈130 ns^{-1}. The ESA of **o*** shows a pronounced peak near 720 nm in CH_2Cl_2, and broader peaks in toluene and benzonitrile (Figure S 11, Figure S 12).

The **g** chromophore absorbs some light at 530 nm (Fig. 1A), ≈3% of the excitations arrives directly at **g*** in **ocg**, which is visible as a small instantaneous rise in the dark green population in Fig. 6C.

It is remarkable that triplet formation by charge recombination occurs in **oc**, but not in **ocg**.

The mechanistic aspects of charge recombination to a local triplet excited state have recently been reviewed [45] and computational studies [46] have shown the importance of the exact conformation of the electron donor acceptor systems. Complementary behaviour of the matrix element for spin orbit coupling and the matrix element for the electronic coupling for charge transfer upon change of conformation has been determined. This is in agreement with a difference in conformation between **oc** and **ocg**.

Spectral evolution in oco, rcr and gcg

In the bichromophoric supramolecular systems an equilibrium between the two possible pinched cone conformations of the calix[4]arene unit is only observed for **oco** in apolar solvents, with one conformation showing a π-stacked sandwich arrangement of the PBI units and the second revealing a non-stacked conformation [36]. This equilibrium is depicted for **oco** in Figure S 3. It is particularly challenging to resolve this equilibrium, since it is notoriously difficult to resolve parallel reactions with many common spectral features. In two solvents, CCl_4 and toluene, evidence was found for the presence of both **oco** conformations in a target analysis of the transient absorption spectra [36]. Here we have refined that target analysis (Figure S 14), resulting in an excellent quality of the fits (Figure S 13). In CCl_4 the sandwich population is larger than that of the non-stacked conformation, cf. the turquoise and magenta solid lines in Fig. 7A. Thus, it was possible to resolve an evolution of the excimer state (turquoise, green, brown in Fig. 7A, B). This evolution likely is present in the ESA and the SE of the excimer. In toluene the sandwich population is smaller than that of the non-stacked conformation, cf. the green and magenta solid lines in Fig. 7C. Still, we could resolve a nice excimer SADS (green spectral trace in Fig. 7D) with the expected bleaches around 490 and 530 nm. The excimer ESA is very broad, extending from 550 to 850 nm. In the more polar solvents CH_2Cl_2 and benzonitrile no evidence for the presence of an excimer was found (Figure S 15). Strikingly, the multiexponential decay of **oco** in CH_2Cl_2 differs from that of **oc**, cf. Fig. 6A. This suggests that the multiexponentiality observed in **oc** in CH_2Cl_2 can be attributed to different conformations. The dimers **rcr** and **gcg** behave similar to their monomeric counterparts **rc** and **gc**, with no evidence for the presence of the stacked conformation (Figure S 16, Figure S 17).

Spectral evolution in rcg and gcrcg

Traces of data and fits at selected wavelengths of **rcg** and **gcrcg** in CH_2Cl_2 after excitation at 530 nm are depicted in Fig. 8. In **rcg** the energy is transferred to **g** within a few ps (black traces, e.g. at 749 nm), and in **gcrcg** the EET rate is about twice as fast (red traces). Straddling time zero is again the coherent artefact, cf. Fig. 4. Again, slight changes of the alignment of the pump and the probe as a function of the delay time in the different experiments are responsible for the apparent differences in the final **g*** decay rate.

In the kinetic scheme of **rcg** (Fig. 9B) all four **r*** states can transfer their energy to the chromophore **g*** (dark green). However, next to this productive EET there is a second loss process, which has not been observed before. Without this process the residuals of the fit show large trends (Figure S 18A,B), whereas with this process the residuals are satisfactory (Figure S 18C,D). This loss process is observed only in the first two excited states $\mathbf{r_1}$* (grey) and $\mathbf{r_2}$* (light green), and must be facilitated by the **g** chromophore, since it is not present in **rc** or **crc**. It results in an **rcg** radical pair (**rcgRP**), with an $\mathbf{r}^{-\cdot}$ radical anion, cf. the absorption in the **rcgRP** SADS from 750 to 800 nm (black in Fig. 10B, Figure S 20) [47], and presumably a $\mathbf{c}^{+\cdot}$ radical cation. In addition, a clear bleach of **r** is present around 575 nm, with smaller bleaches around 450 and 530 nm. This loss amounts to 7%. To resolve this new

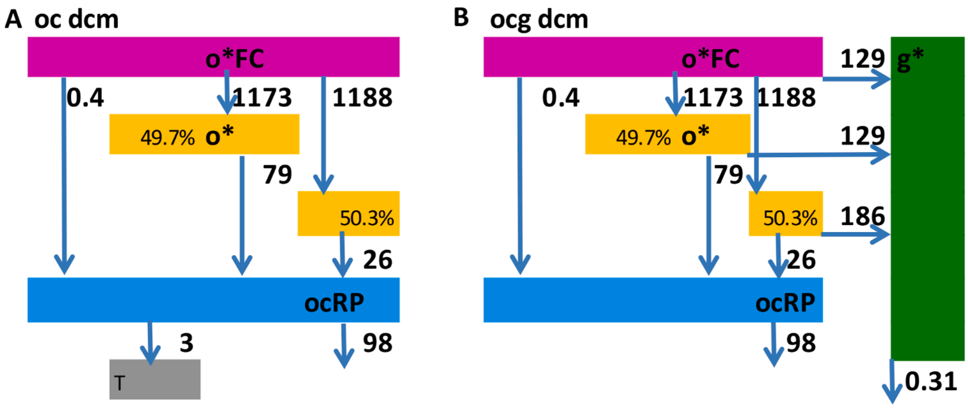

Fig. 5. Kinetic schemes used for the simultaneous target analysis of **oc** (A) and **ocg** (B) in CH_2Cl_2. All rate constants in ns^{-1}. Key: magenta, **o*FC**: excited o chromophore in the Franck-Condon state; orange, two different conformations of **o*** with identical SADS; dark green: **g***; blue, **ocRP**: $\mathbf{c}^{+\cdot}\mathbf{o}^{-\cdot}$ radical ion pair; dark grey, T: triplet. Vertical arrows indicate relaxation of an excited state, or decay. "**ocRP**" is an important loss population formed from **o***. (For interpretation of the references to color in this figure legend, the reader is referred to the web version of this article.)

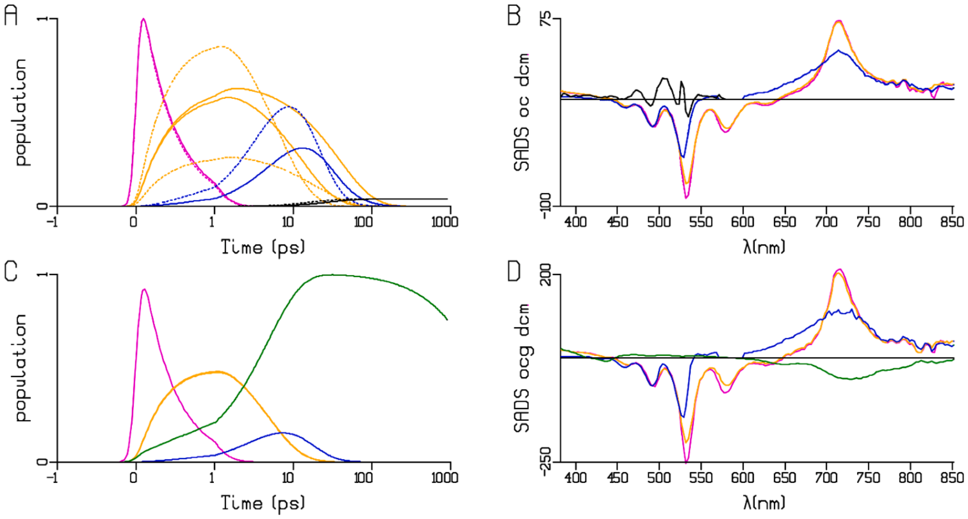

Fig. 6. Populations of the target kinetic schemes from Figure 5 (A,C) and estimated SADS (B,D, in mOD) of **oc** and **ocg** in CH_2Cl_2, respectively. The **oc** and **coc** populations (for the kinetic scheme see Figure S 10) are depicted as solid and dotted lines, respectively. Key: magenta, **o*****FC**: excited **o** chromophore in the Franck-Condon state; orange, two different conformations of **o*** with identical SADS; dark green: **g***; blue, ocRP: $c^{+\cdot}o^{-\cdot}$ radical ion pair; black, triplet excited state on **o**. Note that the triplet SADS (in B) has no contribution above 580 nm.(For interpretation of the references to color in this figure legend, the reader is referred to the web version of this article.)

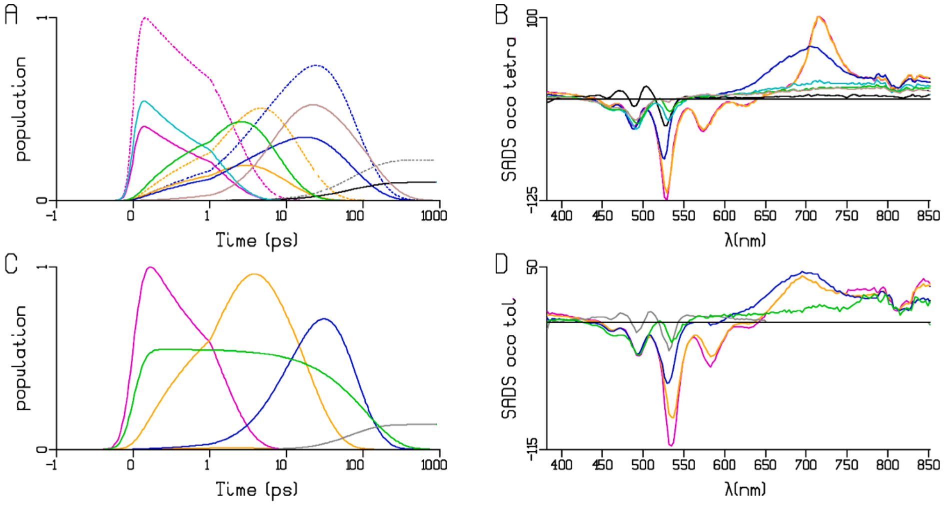

Fig. 7. Populations of the target kinetic schemes from Figure S 14. (A,C) and estimated SADS (B,D, in mOD) of **oco** in CCl_4 and toluene, respectively. In (A) the **oco** and **oc** populations are indicated by solid and dotted lines, respectively. Key non-stacked conformation: magenta, **o*****FC**: excited **o** chromophore in the Franck-Condon state; orange, **o*** relaxed; blue, **ocRP:** $c^{+\cdot}o^{-\cdot}$ radical ion pair; black, grey: triplet in **oco** and **oc**. Key of the π-stacked sandwich arrangement: turquoise, green, brown sequential evolution of the excimer state.(For interpretation of the references to color in this figure legend, the reader is referred to the web version of this article.)

loss-process the simultaneous target analysis taking into account the complete spectral evolution of **r*** was needed. The target analyses of **rcg** in toluene, CH_2Cl_2 and benzonitrile are collated in Figure S 20, demonstrating the presence of the **rcg** radical pair in all three solvents. From the kinetic schemes of **rcg** in the three solvents (Figure S 19) several trends can be discerned. The loss is largest with **rcg** in benzonitrile, 21%, and with **gcrcg** in CH_2Cl_2, 12%. The **rcgRP** decay is slowest in the nonpolar solvent toluene. In **gcrcg** where two acceptors are present the EET rates are about twice as large as in **rcg**. The EET to **g*** is faster from the **r**$_3$***, r**$_4$* states than from **r**$_2$*. This could be due to an increased overlap between the red shifted **r*** emission and the **g** absorption. The **g** chromophore absorbs some light at 530 nm (Fig. 1A), ≈11% of the excitations arrives directly at **g*** in **rcg** and ≈19% in **gcrcg**, which is visible as an instantaneous rise in the dark green populations in Fig. 10A,C.

Spectral evolution in ocr, rcocr and ocrco

The target analyses of **ocr, rcocr** and **ocrco** are summarized in Figure S 21, Figure S 22, and Figure S 23, and detailed for **ocrco** in Fig. 11. The 530 nm light excites both chromophores, the absorption of **o** being about four times as large as that of **r** (Fig. 1A). The **oc** and **r** parts of the kinetic scheme of Figure S 21 are largely consistent with the **oc** and **r** schemes in Figure S 10 and Figure S 19. An additional time constant of ≈500 ps of **r*** relaxation is present (brown in Fig. 11A,B). In all three complexes the **o*** fraction with a smaller rate of **ocRP** formation shows a larger rate of EET to **r***. This fast EET largely circumvents the detrimental loss, resulting in a relatively small population of **ocRP** (blue in Fig. 11A). The estimated SADS (Fig. 11B,D, Figure S 22) are largely consistent with the **oc** and **r** SADS in Fig. 6B and Fig. 10B, respectively. However, the relative amplitudes of the later **r*** SADS differ. Moreover, the SADS of the later **r*** states (brown and purple in Fig. 11B,C,D, Figure S 22, Figure S 23) show features near 490 and 530 nm that can be attributed to the bleach of **o**. This indicates that the later **r*** states are not purely **r***, but may have an excitonic character [48], although there are no features of the **o*** ESA discernible.

Spectral evolution in ocrcg and gcrcocrcg

The target analyses of the most challenging multichromophoric systems **ocrcg** (three chromophores) and **gcrcocrcg** (five chromophores) are described in Figure S 24 and Fig. 12. The quality of the fit is excellent, cf. Figure S 25. Again, the kinetic schemes of Figure S 24 are consistent with those in Figure S 21 and Figure S 19. Note that the estimated SADS from Fig. 10D and Fig. 6B have been used to guide the SADS in Fig. 12. This ensures consistency in shapes and amplitudes, but

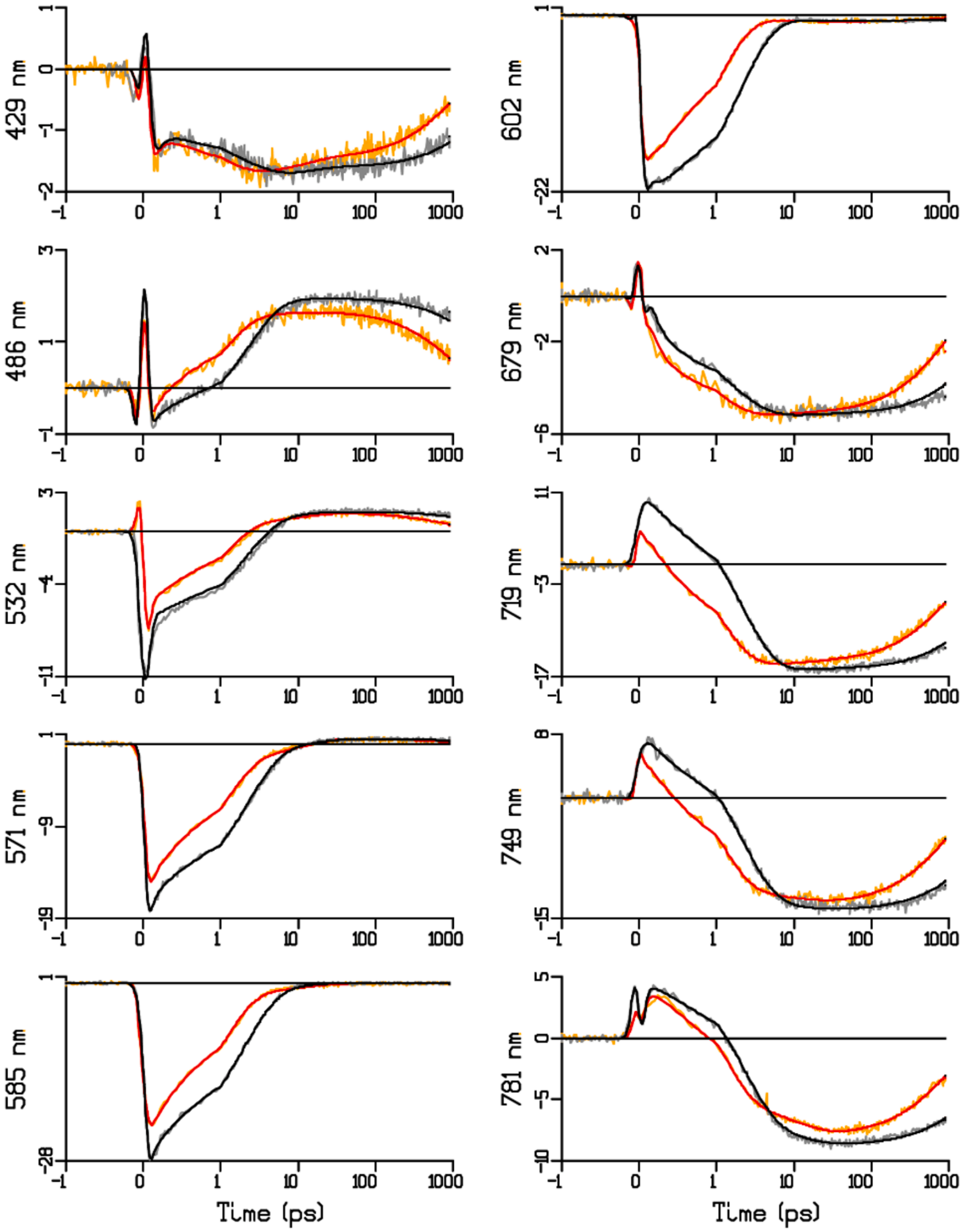

Fig. 8. Selected time traces of **rcg** and **gcrcg** in CH_2Cl_2 after excitation at 530 nm data (in mOD, grey, orange for **rcg** and **gcrcg**, respectively) and fit (black, red). Wavelength is indicated in the ordinate label. Note that the time axis is linear until 1 ps (after the maximum of the IRF), and logarithmic thereafter. The presence of two acceptors in **gcrcg** (orange/red lines) speeds up the EET from **r**.(For interpretation of the references to color in this figure legend, the reader is referred to the web version of this article.)

allows for small experimental variability. Strikingly, the **rcgRP** yield is substantial, ≈20% from the 2nd **r*** state. However, the 50% of the **o*** with a slow rate of **ocRP** formation transfers its energy to the 3rd **r*** state, thus bypassing the 2nd loss process. This is an oversimplification.

When the **r** chromophore in **rcg** is excited, the quantum yield of **g** is 92%, where the loss is due to the **rcgRP** formation. Analogously, when the **o** chromophore in **ocg** is excited, the quantum yield of **g** is 76% due to the **ocRP** formation. In **ocrcg** and **gcrcocrcg** systems the yields are 80% and 82%, respectively. The fast EET from **o*** to **r*** circumvents the **ocRP** formation [35].

It is important to note that we have previously correlated the energy transfer rates to interchromophoric distances based on X-ray structures with an extended conformation [35]. No indications are observed that show a steric factor or π-stacking in the systems discussed in our current work. However, our previous studies on slightly different systems have shown clear effects of proximity. For the **oco** dimers [36] in non-polar solvents (cf. the section Spectral evolution in **oco** above) as well as for a pyrene containing system [49] in tetrahydrofuran solvent clear signatures have been observed in our spectroscopic data for π-stacked conformations (indicating a steric factor).

These clear spectroscopic differences were indicated by excitonic coupling in the UV–vis absorption spectra, ground state bleaching in the fs-TA data showing the excimer state as a ground state depletion (Fig. 7) and broadening of radical anion spectra due to proximity. Such effects are not observed for the **ocg, ocr** and **rcg** based systems in the work presented here.

Conclusions

Accurate determination of loss channels in photo-active molecules and materials is a great challenge. Next to combining different types of experimental techniques, also combining different data sets with identical photoactive units is an excellent approach that can lead to a more accurate description. Simultaneous analysis of multiple data sets that display similar processes ensures a consistent description, and allows for precise quantification of the quantum yields and the photophysical properties. In addition, we have demonstrated that in complexes containing two or more **o** and **r** chromophores excitonic effects may be

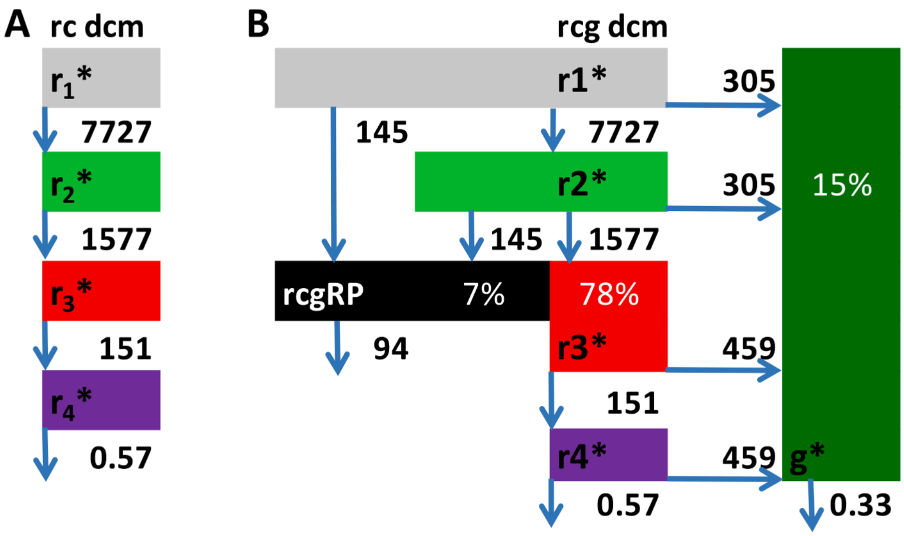

Fig. 9. Kinetic schemes used for the simultaneous target analysis of **rc** (A) and **rcg** (B) in CH_2Cl_2. All rate constants in ns^{-1}. Key: grey, green, red, purple: successively relaxed **r_1***, **r_2***, **r_3***, **r_4***; dark green: **g***; black, **rcgRP**: **rcg** radical pair. Vertical arrows indicate relaxation of an excited state, or decay. **rcgRP** is an important loss population formed from the **r_1*** and **r_2*** state.(For interpretation of the references to color in this figure legend, the reader is referred to the web version of this article.)

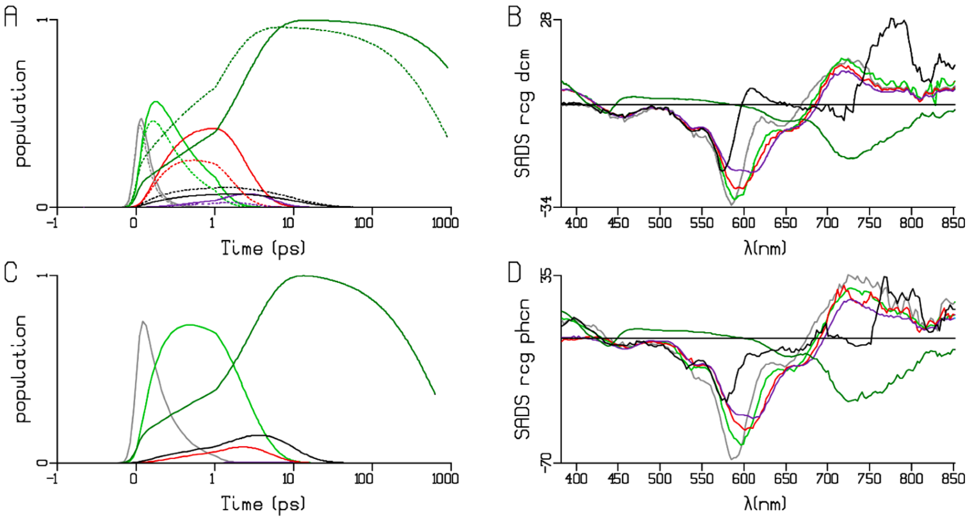

Fig. 10. Populations (A,C) of the target kinetic schemes from Figure 9B and Figure S 19. and estimated SADS (B,D, in mOD) of **rcg** in CH_2Cl_2 and benzonitrile and of **gcrcg** in CH_2Cl_2 (concentrations dotted). Key: grey, green, red, purple: successively relaxed **r_1***, **r_2***, **r_3***, **r_4*** states; dark green: **g***; black, **rcgRP**: **rcg** radical pair. **rcg** shows the typical spectral evolution of the **r** chromophore, as well as EET to **g** (see 730 nm bleach in the **g*** SADS) and **$r^{-\cdot}$** formation, characterized by the 575 nm bleach and the 780 nm absorption (black SADS).(For interpretation of the references to color in this figure legend, the reader is referred to the web version of this article.)

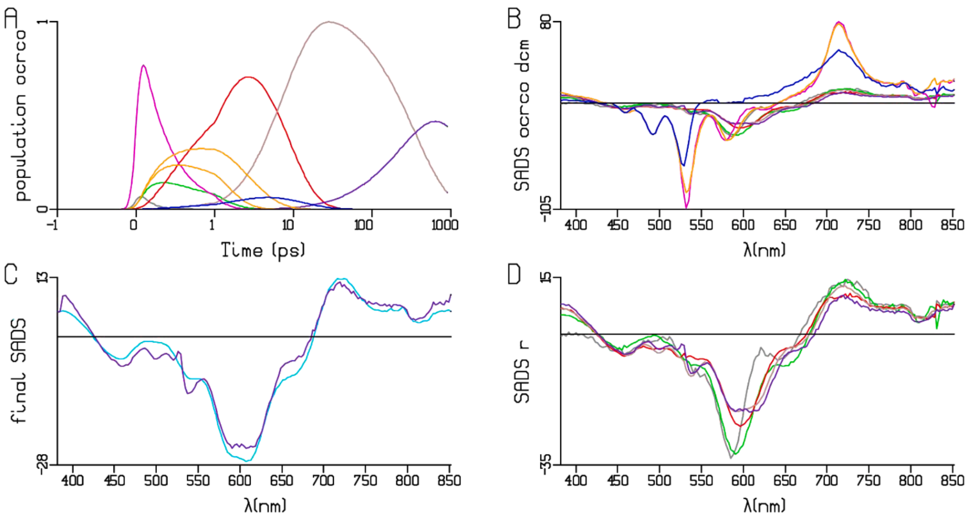

Fig. 11. Populations of the target kinetic schemes from Figure S 21 (A) and estimated SADS (B,D, in mOD) of **ocrco** in CH_2Cl_2. Key: magenta, **o***FC: excited **o** chromophore in the Franck-Condon state; orange, two different conformations of **o*** with identical SADS; blue, **ocRP**: **$c^{+\cdot}o^{-\cdot}$** radical ion pair; grey, green, red, brown, purple: successively relaxed **r*** states. (C) Overlay of the final **r*** SADS from **rc** (cyan) and from **ocrco** in CH_2Cl_2 (purple). Note the **o** bleach features near 490 and 530 nm in (C,D). (For interpretation of the references to color in this figure legend, the reader is referred to the web version of this article.)

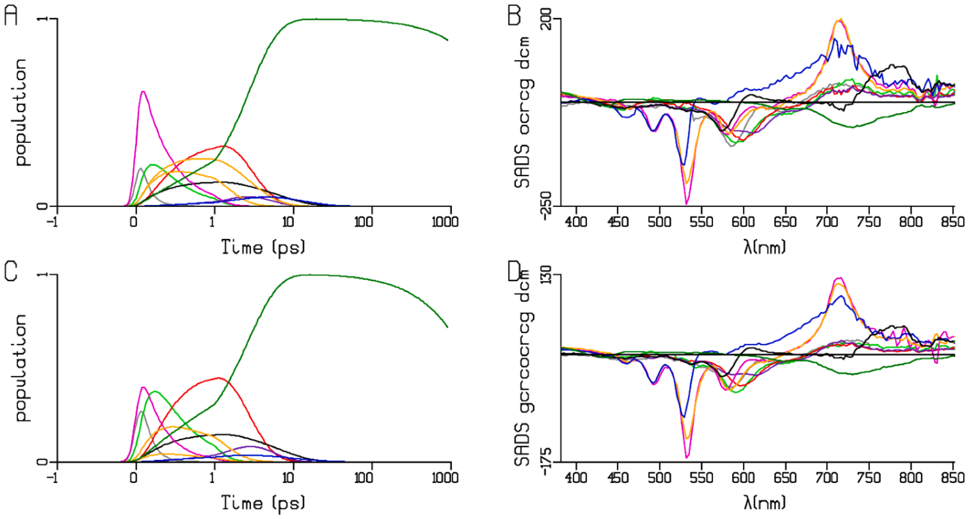

Fig. 12. Populations of the target kinetic schemes from Figure S 24 (A,C) and estimated SADS (B,D, in mOD) of **ocrcg** and **gcrcocrcg** in CH_2Cl_2. All rate constants in ns^{-1}. Key: magenta, **o*FC**: excited **o** chromophore in the Franck-Condon state; orange, two different conformations of **o*** with identical SADS; blue, **ocRP**: $c^{+\cdot}o^{-\cdot}$ radical ion pair; grey, green, red, purple: successively relaxed **r*** states; dark green: **g***; black, **rcgRP**: **rcg** radical pair.(For interpretation of the references to color in this figure legend, the reader is referred to the web version of this article.)

present (cf. Fig. 11, Figure S 22, Figure S 23). The spectral evolution of two possible pinched cone conformations of the calix[4]arene unit in **oco** has been described in two solvents, CCl_4 and toluene.

Nevertheless, to a very large extent the properties of the **oc, or**, and **rcg** building blocks determine the dynamics of EET and RP formation in **ocrcg** (three chromophores) and **gcrcocrcg** (five chromophores). Thus, we have arrived at a consistent kinetic scheme encompassing 12 combinations of the **o, r** and **g** chromophores connected by calix [4] arenes.

Two loss channels in very effective artificial supramolecular light harvesting systems have now been characterized. Their substantial contribution (up to 21%) evidences the need for such elaborate analysis methods.

Data Availability Statement

The data that support the findings of this study are available from the corresponding author upon reasonable request.

There is no conflict of interest to declare.

Declaration of interests

The authors declare that they have no known competing financial interests or personal relationships that could have appeared to influence the work reported in this paper.

Data Availability

Data will be made available on request.

Acknowledgments

We are very grateful to Joris Snellenburg for critical reading and helpful discussions. We are grateful for financial support to the Deutsche Forschungsgemeinschaft (DFG) (Grant Wu 317/4-1), to the Nederlandse Organisatie voor Wetenschappelijk Onderzoek (NWO) (femtosecond equipment) and to the Universiteit van Amsterdam (UvA).

Supplementary materials

Supplementary material associated with this article can be found, in the online version, at doi:10.1016/j.jpap.2022.100154.

References

[1] S. Chu, A. Majumdar, Opportunities and challenges for a sustainable energy future, Nature 488 (2012) 294–303.

[2] R.E. Blankenship, D.M. Tiede, J. Barber, G.W. Brudvig, G. Fleming, M. Ghirardi, M. R. Gunner, W. Junge, D.M. Kramer, A. Melis, T.A. Moore, C.C. Moser, D.G. Nocera, A.J. Nozik, D.R. Ort, W.W. Parson, R.C. Prince, R.T. Sayre, Comparing photosynthetic and photovoltaic efficiencies and recognizing the potential for improvement, Science 332 (2011) 805–809.

[3] R.E. Blankenship, Molecular Mechanisms of Photosynthesis, 2nd ed., Wiley-Blackwell, 2014.

[4] D. Gust, T.A. Moore, A.L. Moore, Solar fuels via artificial photosynthesis, Acc. Chem. Res. 42 (2009) 1890–1898.

[5] A. Gil, M. Medrano, I. Martorell, A. Lázaro, P. Dolado, B. Zalba, L.F. Cabeza, State of the art on high temperature thermal energy storage for power generation. Part 1—concepts, materials and modellization, Renew. Sustain. Energy Rev. 14 (2010) 31–55.

[6] B.C. Thompson, J.M.J. Fréchet, Polymer–fullerene composite solar cells, Angew. Chem. Int. Ed. 47 (2008) 58–77.

[7] J. Hou, O. Inganäs, R.H. Friend, F. Gao, Organic solar cells based on non-fullerene acceptors, Nat. Mater. 17 (2018) 119–128.

[8] A. Armin, W. Li, O.J. Sandberg, Z. Xiao, L. Ding, J. Nelson, D. Neher, K. Vandewal, S. Shoaee, T. Wang, H. Ade, T. Heumüller, C. Brabec, P. Meredith, A history and perspective of non-fullerene electron acceptors for organic solar cells, Adv. Energy Mater. 11 (2021), 2003570.

[9] W. Liu, X. Xu, J. Yuan, M. Leclerc, Y. Zou, Y. Li, Low-bandgap non-fullerene acceptors enabling high-performance organic solar cells, ACS Energy Lett. 6 (2021) 598–608.

[10] R.M. Williams, H.-C. Chen, D. Di Nuzzo, S.C.J. Meskers, R.A.J. Janssen, Ultrafast charge and triplet state formation in diketopyrrolopyrrole low band gap polymer/fullerene blends: influence of nanoscale morphology of organic photovoltaic materials on charge recombination to the triplet state, J. Spectrosc. 2017 (2017), 6867507.

[11] M. Grätzel, Solar energy conversion by dye-sensitized photovoltaic cells, Inorg. Chem. 44 (2005) 6841–6851.

[12] I. Benesperi, H. Michaels, M. Freitag, The researcher's guide to solid-state dye-sensitized solar cells, J. Mater. Chem. C 6 (2018) 11903–11942.

[13] H. Iftikhar, G.G. Sonai, S.G. Hashmi, A.F. Nogueira, P.D. Lund, Progress on electrolytes development in dye-sensitized solar cells, Materials 12 (2019) 1998.

[14] M.A. Green, A. Ho-Baillie, H.J. Snaith, The emergence of perovskite solar cells, Nat. Photon. 8 (2014) 506–514.

[15] D.W. deQuilettes, K. Frohna, D. Emin, T. Kirchartz, V. Bulovic, D.S. Ginger, S. D. Stranks, Charge-carrier recombination in halide perovskites, Chem. Rev. 119 (2019) 11007–11019.

[16] J.Y. Kim, J.-W. Lee, H.S. Jung, H. Shin, N.-G. Park, High-efficiency perovskite solar cells, Chem. Rev. 120 (2020) 7867–7918.

[17] W.-H. Cheng, M.H. Richter, M.M. May, J. Ohlmann, D. Lackner, F. Dimroth, T. Hannappel, H.A. Atwater, H.-J. Lewerenz, Monolithic photoelectrochemical device for direct water splitting with 19% efficiency, ACS Energy Lett. 3 (2018) 1795–1800.

[18] L.A. Muscarella, D. Petrova, R. Jorge Cervasio, A. Farawar, O. Lugier, C. McLure, M.J. Slaman, J. Wang, B. Ehrler, E. von Hauff, R.M. Williams, Air-stable and oriented mixed lead halide perovskite (FA/MA) by the one-step deposition method using zinc iodide and an alkylammonium additive, ACS Appl. Mater. Interfaces 11 (2019) 17555–17562.

[19] A. Kooijman, L.A. Muscarella, R.M. Williams, Perovskite thin film materials stabilized and enhanced by zinc(II) doping, Appl. Sci. 9 (2019) 1678.

[20] K. Nakayama, K. Tanabe, H.A. Atwater, Plasmonic nanoparticle enhanced light absorption in GaAs solar cells, Appl. Phys. Lett. 93 (2008), 121904.
[21] O.D. Miller, E. Yablonovitch, S.R. Kurtz, Strong internal and external luminescence as solar cells approach the Shockley–Queisser limit, IEEE J. Photovolt. 2 (2012) 303–311.
[22] E.D. Kosten, J.H. Atwater, J. Parsons, A. Polman, H.A. Atwater, Highly efficient GaAs solar cells by limiting light emission angle, Light: Sci. Appl. 2 (2013) e45. -e45.
[23] X. Liu, P.R. Coxon, M. Peters, B. Hoex, J.M. Cole, D.J. Fray, Black silicon: fabrication methods, properties and solar energy applications, Energy Environ. Sci. 7 (2014) 3223–3263.
[24] Z. Fan, D. Cui, Z. Zhang, Z. Zhao, H. Chen, Y. Fan, P. Li, Z. Zhang, C. Xue, S. Yan, Recent progress of black silicon: from fabrications to applications, Nanomaterials 11 (2021) 41.
[25] Y. Li, X. Wei, L. Chen, J. Shi, Electrocatalytic hydrogen production trilogy, Angew. Chem. Int. Ed. 60 (2021) 19550–19571.
[26] M. Götz, J. Lefebvre, F. Mörs, A. McDaniel Koch, F. Graf, S. Bajohr, R. Reimert, T. Kolb, Renewable power-to-gas: a technological and economic review, Renew. Energy 85 (2016) 1371–1390.
[27] P.D. Frischmann, K. Mahata, F. Würthner, Powering the future of molecular artificial photosynthesis with light-harvesting metallosupramolecular dye assemblies, Chem. Soc. Rev. 42 (2013) 1847–1870.
[28] Y. Hong, J. Kim, W. Kim, C. Kaufmann, H. Kim, F. Würthner, D. Kim, Efficient multiexciton state generation in charge-transfer-coupled perylene bisimide dimers via structural control, J. Am. Chem. Soc. 142 (2020) 7845–7857.
[29] D. Bialas, E. Kirchner, M.I.S. Röhr, F. Würthner, Perspectives in dye chemistry: a rational approach toward functional materials by understanding the aggregate state, J. Am. Chem. Soc. 143 (2021) 4500–4518.
[30] M.R. Wasielewski, Self-assembly strategies for integrating light harvesting and charge separation in artificial photosynthetic systems, Acc. Chem. Res. 42 (2009) 1910–1921.
[31] H.-C. Chen, D.G.H. Hetterscheid, R.M. Williams, J.I. van der Vlugt, J.N.H. Reek, A. M. Brouwer, Platinum(ii)–porphyrin as a sensitizer for visible-light driven water oxidation in neutral phosphate buffer, Energy Environ. Sci. 8 (2015) 975–982.
[32] M. Bonchio, Z. Syrgiannis, M. Burian, N. Marino, E. Pizzolato, K. Dirian, F. Rigodanza, G.A. Volpato, G. La Ganga, N. Demitri, S. Berardi, H. Amenitsch, D. M. Guldi, S. Caramori, C.A. Bignozzi, A. Sartorel, M. Prato, Hierarchical organization of perylene bisimides and polyoxometalates for photo-assisted water oxidation, Nat. Chem. 11 (2019) 146–153.
[33] J.-W. Kim, H.-S. Kim, G.-H. Yu, Y.-S. Kim, Enhanced photocatalytic activity of 3,4,9,10-perylenetetracarboxylic diimide modified titanium dioxide under visible light irradiation, Bull. Kor. Chem. Soc. 31 (2010) 2849–2853.
[34] C. Hippius, I.H.M. van Stokkum, E. Zangrando, R.M. Williams, F. Würthner, Excited state interactions in calix[4]arene-perylene bisimide dye conjugates: global and target analysis of supramolecular building blocks, J. Phys. Chem. C 111 (2007) 13988–13996.
[35] C. Hippius, I.H.M. van Stokkum, M. Gsanger, M.M. Groeneveld, R.M. Williams, F. Würthner, Sequential FRET processes in calix[4]arene-linked orange-red-green perylene bisimide dye zigzag arrays, J. Phys. Chem. C 112 (2008) 2476–2486.
[36] C. Hippius, I.H.M. van Stokkum, E. Zangrando, R.M. Williams, M. Wykes, D. Beljonne, F. Würthner, Ground- and excited-state pinched cone equilibria in calix[4]arenes bearing two perylene bisimide dyes, J. Phys. Chem. C 112 (2008) 14626–14638.
[37] C. Hippius, Multichromophoric Arrays of Perylene Bisimide Dyes - Synthesis and Optical Properties; Multichromophore Perylenbisimidkaskaden - Synthese und optische Eigenschaften, Universität Würzburg, Fakultät für Chemie und Pharmazie, Würzburg, 2007, pp. 1–237.
[38] I.H.M. van Stokkum, D.S. Larsen, R. van Grondelle, Global and target analysis of time-resolved spectra, Biochim. Biophys. Acta 1657 (2004) 82–104.
[39] I.H.M. van Stokkum, D.S. Larsen, R. van Grondelle, Erratum to "Global and target analysis of time-resolved spectra, Biochim. Biophys. Acta 1658 (2004) 262. -262.
[40] I.H.M. van Stokkum, M. Kloz, D. Polli, D. Viola, J. Weißenborn, E. Peerbooms, G. Cerullo, J.T.M. Kennis, Vibronic dynamics resolved by global and target analysis of ultrafast transient absorption spectra, J. Chem. Phys. 155 (2021), 114113.
[41] S.A. Kovalenko, A.L. Dobryakov, J. Ruthmann, N.P. Ernsting, Femtosecond spectroscopy of condensed phases with chirped supercontinuum probing, Phys. Rev. A 59 (1999) 2369–2384.
[42] P. Osswald, D. Leusser, D. Stalke, F. Würthner, Perylene bisimide based macrocycles: effective probes for the assessment of conformational effects on optical properties, Angew. Chem. Int. Ed. 44 (2005) 250–253.
[43] J. Hofkens, T. Vosch, M. Maus, F. Köhn, M. Cotlet, T. Weil, A. Herrmann, K. Müllen, F.C. De Schryver, Conformational rearrangements in and twisting of a single molecule, Chem. Phys. Lett. 333 (2001) 255–263.
[44] E. Fron, G. Schweitzer, P. Osswald, F. Würthner, P. Marsal, D. Beljonne, K. Müllen, F.C. De Schryver, M. Van der Auweraer, Photophysical study of bay substituted perylenediimides, Photochem. Photobiol. Sci. 7 (2008) 1509–1521.
[45] D.J. Gibbons, A. Farawar, P. Mazzella, S. Leroy-Lhez, R.M. Williams, Making triplets from photo-generated charges: observations, mechanisms and theory, Photochem. Photobiol. Sci. 19 (2020) 136–158.
[46] S. Bissesar, D.M.E. van Raamsdonk, D.J. Gibbons, R.M. Williams, Spin orbit coupling in orthogonal charge transfer states: (TD-)DFT of pyrene—dimethylaniline, Molecules 27 (2022) 891.
[47] A. Sautter, B.K. Kaletas, D.G. Schmid, R. Dobrawa, M. Zimine, G. Jung, I.H.M. van Stokkum, L. De Cola, R.M. Williams, F. Würthner, Ultrafast energy-electron transfer cascade in a multichromophoric light-harvesting molecular square, J. Am. Chem. Soc. 127 (2005) 6719–6729.
[48] I.H.M. van Stokkum, C.C. Jumper, T.S. Lee, M. Myahkostupov, F.N. Castellano, G. D. Scholes, Vibronic and excitonic dynamics in perylenediimide dimers and tetramer, J. Chem. Phys. 153 (2020), 224101.
[49] N. Van Anh, F. Schlosser, M.M. Groeneveld, I.H.M. van Stokkum, F. Würthner, R. M. Williams, Photoinduced interactions in a pyrene-calix[4]arene-perylene bisimide dye system: probing ground-state conformations with excited-state dynamics of charge separation and recombination, J. Phys. Chem. C 113 (2009) 18358–18368.